Letter

Strain-induced lateral heterostructures: Hole localization and the emergence of flat bands in rippled MoS_2 monolayers

Meshal Alawein,[1,2] Joel W. Ager,[2,3] Ali Javey,[1,2] and D. C. Chrzan[2,3,*]

[1]*Electrical Engineering and Computer Science, University of California, Berkeley, California 94720, USA*
[2]*Materials Sciences Division, Lawrence Berkeley National Laboratories, Berkeley, California 94720, USA*
[3]*Materials Science and Engineering, University of California, Berkeley, California 94720, USA*

(Received 27 October 2024; revised 22 January 2025; accepted 11 February 2025; published 25 February 2025)

The formation of 2D lateral heterostructures in rippled MoS_2 and similar transition metal dichalcogenides (TMDs) is studied using density functional theory. Compression of rippled TMDs beyond a threshold compression leads to the formation of a flat valence band associated with strongly localized holes. The implications for exciton manipulation and the emergence of one-dimensional heavy fermion behavior are discussed.

DOI: 10.1103/PhysRevMaterials.9.L021002

The study of the electronic properties of van der Waals (vdW) 2D materials remains a fruitful area for uncovering new material behaviors [1]. A prime example is the discovery of superconductivity in moiré-patterned bilayer graphene, driven by the formation of flat bands near the Fermi level at a specific "magic" twist angle ($\sim$1.1°) [2]. These flat bands arise from the unique stacking and specific rotational alignment between the two layers, which creates a moiré superlattice—a long-wavelength periodic pattern that profoundly modifies the electronic band structure. The overlapping periodic potentials from the slightly misaligned graphene layers cause the electronic states to localize, effectively flattening the bands, resulting in a high density of states and reduced kinetic energy of electrons. The slowed electron motion in these flat bands enhances carrier correlations providing a fertile ground for exploring exotic quantum phenomena such as superconductivity [3–13], magnetism [14–21], linear-in-temperature resistivity [22–24], intrinsic quantized anomalous Hall effect [25–27], and correlated insulating phases [3,28–36]. The direct visualization of these flat bands [37] has confirmed their critical role in driving the rich phase diagram observed in twisted bilayer graphene, making it a cornerstone in the emerging field of "twistronics" [38].

Beyond bilayer graphene, moiré flat bands have also been observed in other vdW 2D materials, notably in γ-graphyne [39], hBN [40], and transition metal dichalcogenides (TMDs) [41–45]. Nevertheless, the magic angle phenomenon seems to be unique to twisted bilayer semimetals. Materials such as hBN, MoS_2, and γ-graphyne do not exhibit a critical angle-dependent transition. Instead, flat bands in these materials emerge at under more relaxed conditions. In particular, flat bands result at sufficiently small twist angles, where the electronic bandwidth becomes comparable to or smaller than the Coulomb interaction energy, leading to similarly rich physics as in twisted bilayer graphene. For example, twisted bilayer WSe_2 exhibits flat bands at twist angles between about 4° and 5° [46], and WSe_2/WS_2 shows different localization patterns depending on the angle, as confirmed by scanning tunneling microscopy and spectroscopy [47]. Moreover, the study of flat band plasmons in twisted bilayer MoS_2 [48], as well as the role of spin-orbit coupling in TMD heterobilayers [49] highlights the broader relevance of flat bands across various TMDs and underscores the diverse electronic behaviors that flat bands can induce in these materials.

While the mechanical properties (including buckling) of vdW 2D materials under strain have been extensively studied [50–54], the effects of periodic rippling on band structure and transport have not been explored in detail. Shi *et al.* [55] demonstrated that buckling of a $MoSe_2$ monolayer leads to formation of dipole moments (i.e., flexoelectricity). Qi *et al.* predicted that the band gap of MoS_2 could be tuned by the combination of the compression and the application of an electric field [56]. Presumably, the electric field couples to the dipole moments that are induced by the bending, and this alters the electronic structure. This work noted a direct/indirect transition at a critical curvature for ripples described by a k vector in the zig-zag direction, but did not observe a transition for the equivalent armchair ripples. The properties of the carriers in the flat bands [57,58] were not discussed, nor was the potential for heterostructure behavior explored in any detail. More recent work, incorporating spin-orbit coupling, finds that rippling can lead to dark excitons [59].

In the present study, the impact of uniaxial compression, including buckling, along the armchair direction on the electronic structure of MoS_2 and other TMD monolayers is presented. This study is motivated by the fact that the band gap of TMD monolayers depends on strain [60]. This implies that spatial variations in strain will result in spatial variations in the band gap, effectively creating a strain-determined heterostructure. We hypothesize that bending will similarly affect the band gap, with spatial variations in bending stress leading to the formation of a strain-defined lateral heterostructure. Using *ab initio* density functional theory (DFT) calculations, feasibility of creating strain-induced 2D heterostructures is explored directly in MoS_2, WS_2, $MoSe_2$, and WSe_2. Notably, in MoS_2 and WS_2, these heterostructures exhibit substantial hole localization for compression in the armchair direction

*Contact author: dcchrzan@berkeley.edu

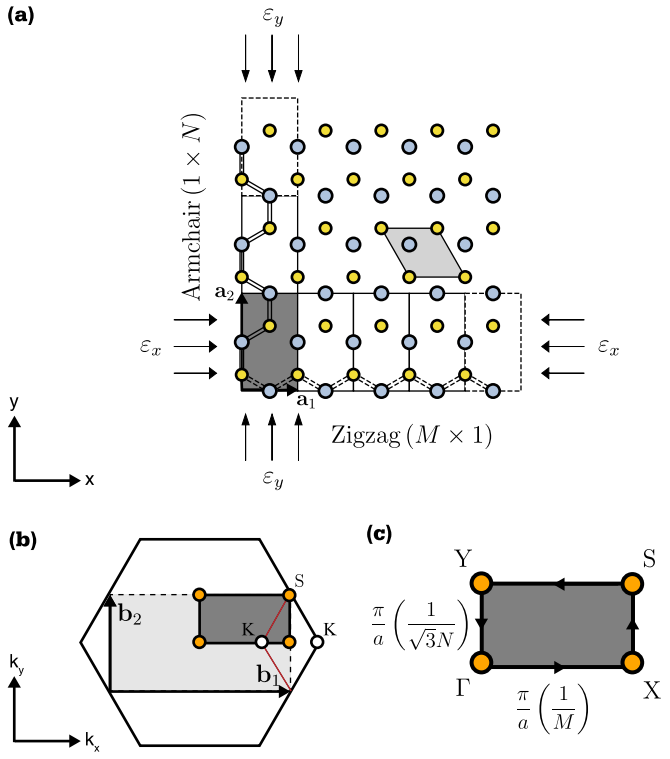

FIG. 1. Direct- and reciprocal-space lattices of 1H-MoS_2. (a) The crystal in real space. Dark and light gray circles represent Mo and S atoms, respectively. The primitive cell is shown in light gray, and the nonprimitive rectangular cell that forms the basis of the rippled structures is shown in dark gray. (b) The Brillouin zone for the primitive and nonprimitive unit cells of the 2D crystal. The irreducible wedge of the nonprimitive zone is highlighted in dark gray. (c) The irreducible wedge for the $M \times N$ supercell Brillouin zone.

at compressions less than their Se-containing counterparts. Therefore, the focus of this study is chosen to be MoS_2.

Physically, the ripples break the threefold symmetry of the flat monolayer, and will thus impact all of the tensor properties of the material. In particular, one expects that both the thermal and electrical conductivity will become anisotropic in the rippled monolayer. In the case of electronic conductivity, it is shown in the following that rippling can lead to the formation of a strain-induced lateral heterostructure, with holes localized at the strongly curved troughs and peaks of the sinusoidal buckling pattern.

Interestingly, the valence bands in these heterostructures become remarkably flat. The ability to induce flat bands through controlled compression adds to the diverse toolkit available for band engineering, expanding the range of materials and structures where such phenomena can be studied. By exploring strain as a means to achieve flat band effects, we aim to contribute to the broader understanding of quantum phenomena in 2D materials, building on the exciting developments already achieved through other methods like twisting bilayers.

MoS_2 consists of repeating vdW bonded two-layer units, where each layer is made up of covalently bonded S-Mo-S sandwiches. The monolayer in its most naturally abundant hexagonal polytype (1H-MoS_2) is depicted in Fig. 1. For this paper, we focus on compression applied parallel to the armchair direction, which corresponds to the y axis in our case. To study the impact of uniaxial compression, we generated buckled cells using the LAMMPS code [61], employing the reactive empirical bond order (REBO) potential [62,63]. The monolayer was subjected to incremental compression along the armchair direction (y axis). We define the compression in percent to be $C = -100\frac{\Delta L}{L_0} = 1, 2, \ldots, 20\%$. Here ΔL is nominal change in length of the compressed structure, and L_0 is the equilibrium length of the flat structure (at zero temperature). Structural relaxation is carried out at each step using a conjugate gradient algorithm. A vacuum region greater than 20 Å was employed in all calculations to eliminate spurious interactions between periodically repeated cells.

The buckled cells obtained from LAMMPS were then used as starting points for DFT studies using the SIESTA package [64]. The generalized gradient approximation (GGA) with the Perdew-Burke-Ernzerhof (PBE) parametrization was used to treat exchange-correlation effects [65]. Norm-conserving pseudopotentials and a double-zeta polarized basis set were employed to describe the electron-ion interactions. Structures are fully relaxed until the force on each atom is less than 0.01 eV/Å. For the self-consistent field (SCF) cycle, convergence criteria of $\Delta\hat{\rho} = 10^{-5}$ and $\Delta\hat{H} = 10^{-4}$ eV were used for density and Hamiltonian matrices, respectively. A finite electronic smearing temperature of $T_e = 300$ K was used for the Fermi-Dirac occupation function to aid in convergence in the case the system became metallic. The real-space grid energy cutoff was set to 300 Ry. A Γ-centered Monkhorst-Pack k-point mesh was used to sample the 2D Brillouin zone (BZ), employing a minimum of an 8×6 k-point mesh. The electronic band structures and density of states were calculated to analyze the effects of periodic wrinkling on the electronic properties of the MoS_2 monolayers. We studied the properties of 1×10 and 1×20 rippled structures. The structure of the $1 \times N$ unit cells is defined in Fig. 1(a).

Figure 1(b) shows the Brillouin zone for the 1×1 unit cell is embedded within the Brillouin zone for the primitive unit cell. Figure 1(c) shows the irreducible wedge of the Brillouin zone for the $M \times N$ rippled structure, labeling the high-symmetry points. Note that for $1 \times N$ structures, the width of this wedge remains fixed at $\frac{\pi}{a}$, and the height decreased with increasing N. Band structures for the 1×10 case are plotted in Fig. 2 for six compressions chosen to highlight notable features of the electronic structure as described below.

First, the material undergoes direct-to-indirect transition (Fig. 2). Under zero compression, the band gap is predicted to be direct and located at the K point. Initially, the gap increases with increasing compression. Upon buckling, however, the gap starts to decrease with increasing compression. As the structures compress further and buckle, the valence band along Γ → K begins to flatten and increases in energy relative to the valence band maximum (VBM). At a compression between 7% and 8%, the valence band maximum shifts to Γ, rendering the material indirect.

Second, compression can be used to tune the band gap. Figure 3(a) shows the band gap as a function of compression 1×10 and 1×20 structures. The gap decreases more rapidly with compression for the shorter wavelength buckled structure, suggesting that the gap is correlated with the maximum

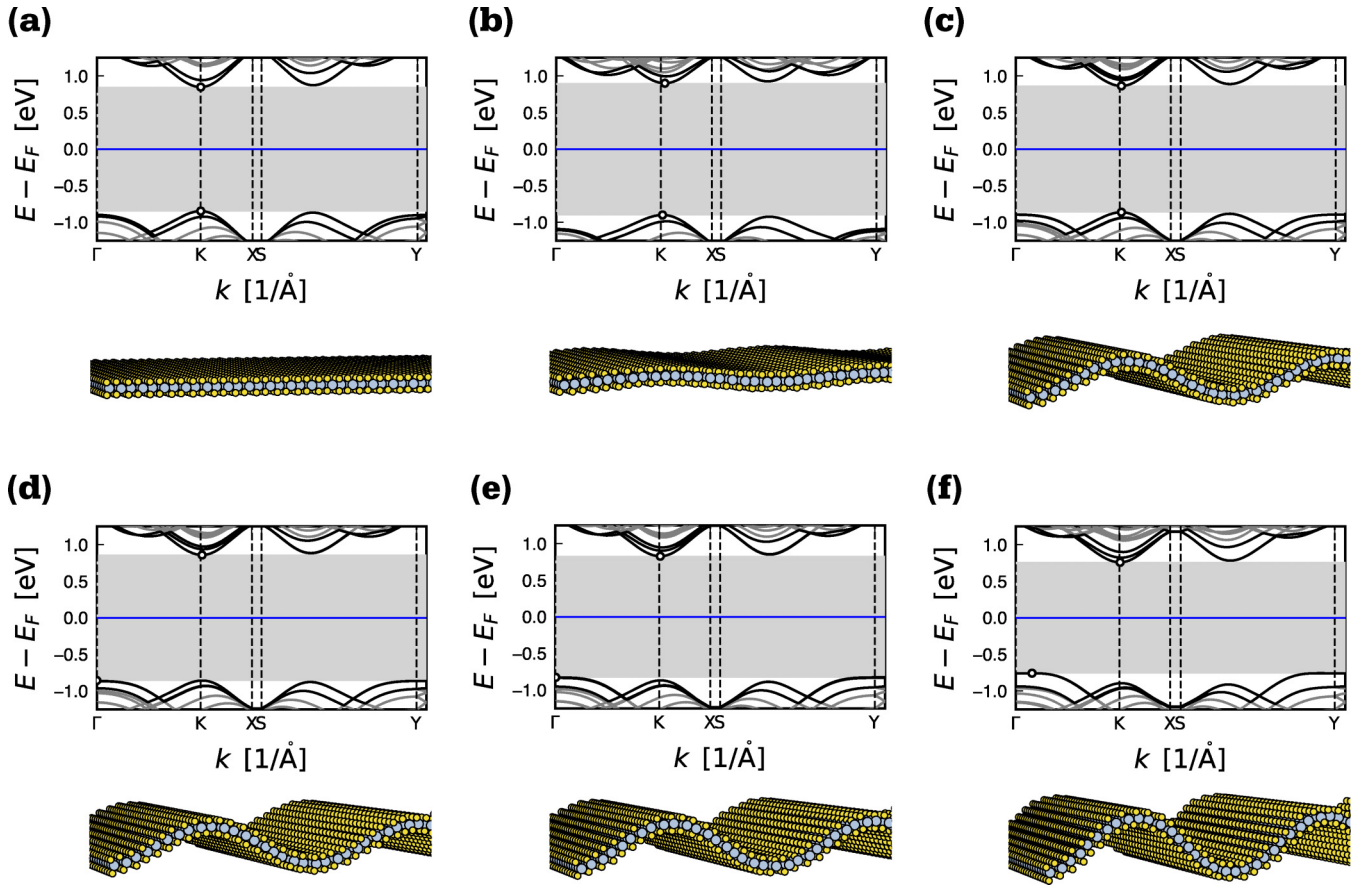

FIG. 2. The structure and band structures for the 1×10 structures plotted for different compressions: (a) 0%, (b) 3%, (c) 7%, (d) 8%, (e) 10%, and (f) 15%. The open symbols indicate the computed VBM (valence band maximum) and CBM (conduction band minimum). The rippled structure undergoes a direct-indirect transition between 7% and 8% compression. At this transition, the holes become localized, as evidenced by the flat band at Γ.

curvature of the structures. The maximum curvature was calculated by fitting a smooth curve through the positions of the Mo atoms, and then obtaining the maximum curvature from the resulting curve. Figure 3(b) plots the maximum bending curvature (κ) for the structures as a function of compression. Like the gap, the maximum bending curvature increases with compression more rapidly in the 1×10 structure than in the 1×20 structure, indicating a correlation between the gap and the maximum bending curvature.

Figures 3(c)–3(f) plot the effective masses for the VBM and the conduction band minimum (CBM). At lower compressions, the effective masses gradually change with compression. However, between 7% and 8% compression for the 1×10 case (and between 12% and 13% for the 1×20 case), there is a dramatic increase in the magnitude of the effective mass of the holes. This increase is triggered by the direct-to-indirect band transition in which the VBM switches to the Γ point. As compression continues, the maximum shifts off of Γ, but the relevant band remains very flat, making the computation of the effective mass difficult, as the bands have nearly zero curvature. Interestingly, the mass of the holes increases in both principal directions, but the magnitude of the *yy* component of the mass is always larger than the magnitude of the *xx* component (See the Supplemental Material [66]).

The band crossing transition is associated with the localization of the holes. Figure 4 shows the electron density probability distributions for the states at the VBM and CBM for compressions of the 1×10 MoS_2 cell. For compressions below the direct-to-indirect transition, the VBM and CBM states are distributed nearly uniformly throughout the structure. However, for compressions greater than that associated with the direct-to-indirect transition, the VBM states are clearly localized to the regions with the highest bending curvature. Moreover, inspection of the figures for MoS_2 suggests that the holes are localized to a mixture of the $3d_{z^2}$ orbital of the Mo and the $3p$ orbitals of the S atoms on the tensile side of the bent film. However, the CBM states remain distributed throughout the film at all compressions studied. The buckled structure, in this sense, has become a lateral heterostructure with the different materials defined by the local bending curvature—highly curved regions are the material confining the holes, and the flat regions near the inflection points of the buckled structures becomes the second material of the heterostructure.

In the plot of the electron density distribution, the states are localized at the peaks and valleys of the rippled structure. However, this plot includes contributions from multiple k points. If one considers the contribution from a single k point, one finds that the states are either localized at the peaks

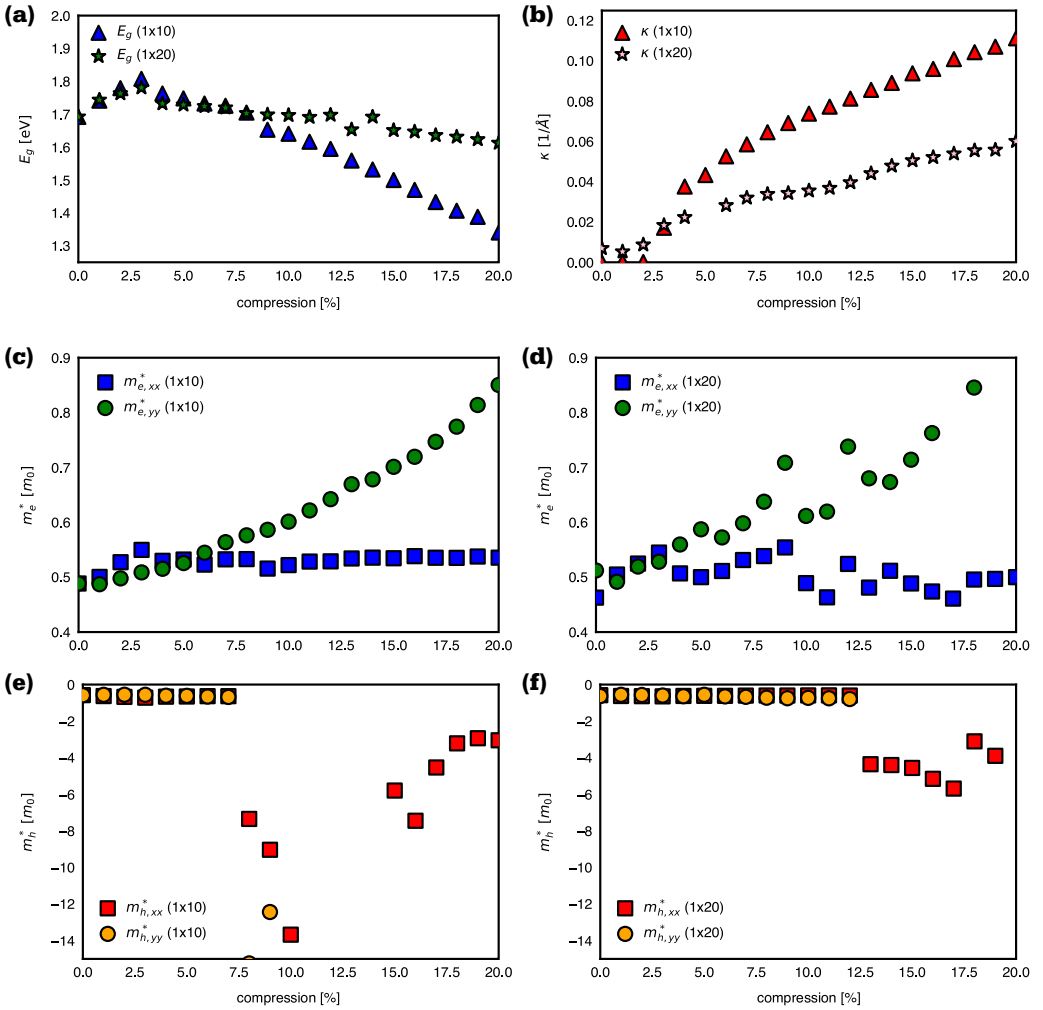

FIG. 3. (a) The band gap as a function of compression for both the 1×10 and 1×20 structures. (b) The maximum curvature in the film plotted as a function of compression for both the 1×10 and 1×20 structures. (c) The effective mass of the electrons at the CBM plotted as a function of compression for the 1×10 structure. (d) The effective mass of the electrons at the CBM plotted as a function of compression for the 1×20 structure. (e) The effective mass of the holes at the VBM plotted as a function of compression for the 1×10 structure. At the direct-indirect transition, the magnitude of the hole mass increases dramatically in both the x and y directions, though the holes are more massive in the y direction. (f) The effective mass of the holes at the VBM plotted as a function of compression for the 1×20 structure. At the direct-indirect transition, the magnitude of the hole mass increases dramatically in both the x and y directions, though the holes are more massive in the y direction.

or at the valleys of the ripples, but not both. Specifically, there are degenerate states occupying either the valleys or the peaks alone that, when considered as a whole, maintain the peak/valley symmetry in the charge density.

To explore whether or not hole localization upon sufficient bending is a general feature of TMDs, we computed the band structures and probability densities of the states at the VBM and CBM for 1×10 WS_2, $MoSe_2$, and WSe_2 under compression. (See the Supplemental Material [66] for band structures and probability density plots). The band structures all display a similar compression driven band-crossing transition, though the two S containing compounds show the band crossing transition at lower compressions. The bands of the S-containing compounds also appear flatter than those for the Se-containing compounds. The probability densities all show similar hole localization after the band-crossing transition. The implication is that buckling induced lateral heterostructures are possible in all four materials.

The emergence of flat bands in compressed and buckled MoS_2 monolayers is an intriguing phenomenon resulting from the strain-induced modulation of the electronic band structure. By comparing the behaviors of the 1×10 and 1×20 structures, one can identify two key factors that appear to govern the compression at which localization occurs. First, the local curvature at the peaks and valleys alters the electronic states at these points compared to their properties within the flat structure. The more sharply bent, the more significant the alteration in the electronic structure. Second, the changes in the electronic structure lead to localization of the states within the structure. The associated localization length appears to decrease with increasing curvature. True localization of the states occurs when the localization length is shorter than the

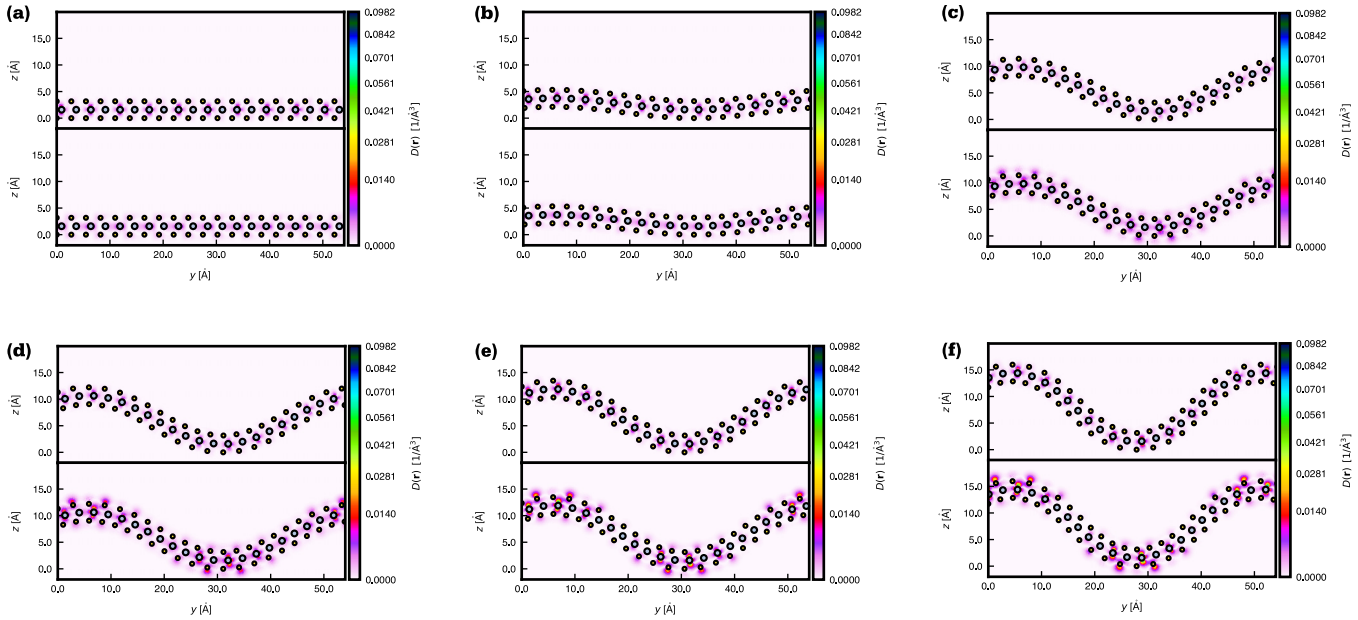

FIG. 4. The probability density arising from the states near (top) CBM and bottom (VBM) for compressions (a) 0%, (b) 3%, (c) 7%, (d) 8%, (e) 10%, and (f) 15%. From the figures it is clear that the holes become localized to the regions of maximum curvature, and in particular on the Mo $3d_{z^2}$ and the S $2p$ states. In contrast, the electrons remain essentially delocalized through the compression range shown.

wavelength of the buckled state. Thus, localization occurs at a smaller curvature for the 1×20 structure than for the 1×10 structure because the distance between valleys and peaks is larger in the 1×20 structure.

The flat bands observed in these rippled structures are analogous to those found in moiré-patterned bilayer graphene and twisted bilayer TMDs, where the interplay between electronic bandwidth and Coulomb interactions gives rise to strongly correlated electronic states. However, in the case of rippled MoS_2, the flat bands are induced by buckling and the bending of the films rather than stacking or twisting, potentially providing an alternative route to engineering exotic electronic phases. The resulting electronic structure of the rippled states resembles that of a lateral heterostructure, where the localized holes are confined to the peaks and valleys of the ripples, effectively forming quantum wells. Indeed, localization of holes might also lead to exciton trapping, a phenomenon that could be tuned using strain and exploited for device development.

Periodic rippling in TMD monolayers induces a systematic symmetry reduction, transitioning from the high-symmetry $p3m1$ plane group and $\bar{6}2m$ (D_{3h}) point group in the flat state to the cm plane group and $2m$ (C_{2v}) point group under compression, and ultimately to the pm plane group and m (C_s) point group in the buckled state. This reduction eliminates a sixfold rotoinversion axis, and may introduce a glide operation (for even N). The result is a dramatically altered Brillouin zone. Specifically, the buckling introduces a long wavelength periodicity that reorganizes the electronic structure into minibands. The curvature modulation localizes electronic states at high-curvature regions, producing flat bands driven entirely by intralayer strain and bending. Unlike twisted bilayer graphene, where flat bands arise from interlayer moiré patterns that partially retain hexagonal symmetry (e.g., D_6 or D_3 depending on the twist angle), rippled TMDs achieve flat bands through complete loss of hexagonal symmetry and more pronounced Brillouin zone folding. These unique intralayer effects create tunable electronic and thermal anisotropies, with the compressed crystal exhibiting distinct properties along and perpendicular to the ripple axis, transitioning from isotropic 2D to quasi-1D behavior.

In particular, the localization is accompanied by a strongly anisotropic hole mass. The magnitudes of the hole mass at the band crossing transition are nearly three times larger in the y direction than they are in the x direction (see the Supplemental Material [66]). The implication is that the holes are confined more strongly in the y direction than they are in the x direction. This suggests that the peaks and valleys of the rippled structures become, effectively, 1D heavy fermion conductors if sufficiently (p type) doped [67]. If so, rippled TMDs may serve as model tunable systems for the study of 1D highly correlated materials.

In conclusion, we have studied the electronic properties of rippled TMDs using density functional theory. We find that the symmetry breaking due to the ripples leads to the formation of strain-determined 2D lateral heterostructures. These heterostructures are characterized by holes localized near the regions of maximum bending curvature, while electrons remain itinerant. This suggests that strain engineering using ripples can be a powerful tool for tailoring the electronic properties of 2D materials, offering new possibilities for advanced electronic and optoelectronic devices. These findings also suggest the rippled TMDs might serve as a model system for the study of 1D heavy fermion materials.

The authors acknowledge the support of the US Department of Energy, Office of Science, Office of Basic Energy Sciences, Materials Sciences and Engineering Division under Contract No. DE-AC02-05Ch11231 (Electronic Materials program).

[1] J. T. Gish, D. Lebedev, T. W. Song, V. K. Sangwan, and M. C. Hersam, Van der waals opto-spintronics, Nat. Electron. **7**, 336 (2024).

[2] R. Bistritzer and A. H. MacDonald, Moiré bands in twisted double-layer graphene, Proc. Natl. Acad. Sci. USA **108**, 12233 (2011).

[3] H. C. Po, L. Zou, A. Vishwanath, and T. Senthil, Origin of Mott insulating behavior and superconductivity in twisted bilayer graphene, Phys. Rev. X **8**, 031089 (2018).

[4] Y. Cao, V. Fatemi, S. Fang, K. Watanabe, T. Taniguchi, E. Kaxiras, and P. Jarillo-Herrero, Unconventional superconductivity in magic-angle graphene superlattices, Nature (London) **556**, 43 (2018).

[5] H. Isobe, N. F. Q. Yuan, and L. Fu, Unconventional superconductivity and density waves in twisted bilayer graphene, Phys. Rev. X **8**, 041041 (2018).

[6] F. Wu, A. H. MacDonald, and I. Martin, Theory of phonon-mediated superconductivity in twisted bilayer graphene, Phys. Rev. Lett. **121**, 257001 (2018).

[7] B. Lian, Z. Wang, and B. A. Bernevig, Twisted bilayer graphene: A phonon-driven superconductor, Phys. Rev. Lett. **122**, 257002 (2019).

[8] Y.-Z. Chou, Y.-P. Lin, S. D. Sarma, and R. M. Nandkishore, Superconductor versus insulator in twisted bilayer graphene, Phys. Rev. B **100**, 115128 (2019).

[9] E. Codecido, Q. Wang, R. Koester, S. Che, H. Tian, R. Lv, S. Tran, K. Watanabe, T. Taniguchi, F. Zhang *et al.*, Correlated insulating and superconducting states in twisted bilayer graphene below the magic angle, Sci. Adv. **5**, eaaw9770 (2019).

[10] M. Yankowitz, S. Chen, H. Polshyn, Y. Zhang, K. Watanabe, T. Taniguchi, D. Graf, A. F. Young, and C. R. Dean, Tuning superconductivity in twisted bilayer graphene, Science **363**, 1059 (2019).

[11] Y. Saito, J. Ge, K. Watanabe, T. Taniguchi, and A. F. Young, Independent superconductors and correlated insulators in twisted bilayer graphene, Nat. Phys. **16**, 926 (2020).

[12] G. Shavit, E. Berg, A. Stern, and Y. Oreg, Theory of correlated insulators and superconductivity in twisted bilayer graphene, Phys. Rev. Lett. **127**, 247703 (2021).

[13] M. Oh, K. P. Nuckolls, D. Wong, R. L. Lee, X. Liu, K. Watanabe, T. Taniguchi, and A. Yazdani, Evidence for unconventional superconductivity in twisted bilayer graphene, Nature (London) **600**, 240 (2021).

[14] L. A. Gonzalez-Arraga, J. L. Lado, F. Guinea, and P. San-Jose, Electrically controllable magnetism in twisted bilayer graphene, Phys. Rev. Lett. **119**, 107201 (2017).

[15] A. O. Sboychakov, A. V. Rozhkov, A. L. Rakhmanov, and F. Nori, Externally controlled magnetism and band gap in twisted bilayer graphene, Phys. Rev. Lett. **120**, 266402 (2018).

[16] A. L. Sharpe, E. J. Fox, A. W. Barnard, J. Finney, K. Watanabe, T. Taniguchi, M. A. Kastner, and D. Goldhaber-Gordon, Emergent ferromagnetism near three-quarters filling in twisted bilayer graphene, Science **365**, 605 (2019).

[17] T. M. R. Wolf, J. L. Lado, G. Blatter, and O. Zilberberg, Electrically tunable flat bands and magnetism in twisted bilayer graphene, Phys. Rev. Lett. **123**, 096802 (2019).

[18] S.-Y. Li, Y. Zhang, Y.-N. Ren, J. Liu, X. Dai, and L. He, Experimental evidence for orbital magnetic moments generated by moiré-scale current loops in twisted bilayer graphene, Phys. Rev. B **102**, 121406(R) (2020).

[19] R. Pons, A. Mielke, and T. Stauber, Flat-band ferromagnetism in twisted bilayer graphene, Phys. Rev. B **102**, 235101 (2020).

[20] L. Klebl, Z. A. H. Goodwin, A. A. Mostofi, D. M. Kennes, and J. Lischner, Importance of long-ranged electron-electron interactions for the magnetic phase diagram of twisted bilayer graphene, Phys. Rev. B **103**, 195127 (2021).

[21] J. Vahedi, R. Peters, A. Missaoui, A. Honecker, and G. T. de Laissardière, Magnetism of magic-angle twisted bilayer graphene, SciPost Phys. **11**, 083 (2021).

[22] H. Polshyn, M. Yankowitz, S. Chen, Y. Zhang, K. Watanabe, T. Taniguchi, C. R. Dean, and A. F. Young, Large linear-in-temperature resistivity in twisted bilayer graphene, Nat. Phys. **15**, 1011 (2019).

[23] F. Wu, E. Hwang, and S. D. Sarma, Phonon-induced giant linear-in-T resistivity in magic angle twisted bilayer graphene: Ordinary strangeness and exotic superconductivity, Phys. Rev. B **99**, 165112 (2019).

[24] Y. Cao, D. Chowdhury, D. Rodan-Legrain, O. Rubies-Bigorda, K. Watanabe, T. Taniguchi, T. Senthil, and P. Jarillo-Herrero, Strange metal in magic-angle graphene with near planckian dissipation, Phys. Rev. Lett. **124**, 076801 (2020).

[25] M. Serlin, C. L. Tschirhart, H. Polshyn, Y. Zhang, J. Zhu, K. Watanabe, T. Taniguchi, L. Balents, and A. F. Young, Intrinsic quantized anomalous Hall effect in a moiré heterostructure, Science **367**, 900 (2020).

[26] N. Bultinck, S. Chatterjee, and M. P. Zaletel, Mechanism for anomalous Hall ferromagnetism in twisted bilayer graphene, Phys. Rev. Lett. **124**, 166601 (2020).

[27] J. Liu and X. Dai, Theories for the correlated insulating states and quantum anomalous Hall effect phenomena in twisted bilayer graphene, Phys. Rev. B **103**, 035427 (2021).

[28] Y. Cao, V. Fatemi, A. Demir, S. Fang, S. L. Tomarken, J. Y. Luo, J. D. Sanchez-Yamagishi, K. Watanabe, T. Taniguchi, E. Kaxiras *et al.*, Correlated insulator behaviour at half-filling in magic-angle graphene superlattices, Nature (London) **556**, 80 (2018).

[29] N. F. Q. Yuan and L. Fu, Model for the metal-insulator transition in graphene superlattices and beyond, Phys. Rev. B **98**, 045103 (2018).

[30] B. Padhi, C. Setty, and P. W. Phillips, Doped twisted bilayer graphene near magic angles: Proximity to wigner crystallization, not Mott insulation, Nano Lett. **18**, 6175 (2018).

[31] M. Ochi, M. Koshino, and K. Kuroki, Possible correlated insulating states in magic-angle twisted bilayer graphene under strongly competing interactions, Phys. Rev. B **98**, 081102(R) (2018).

[32] Y. Zhang, K. Jiang, Z. Wang, and F. Zhang, Correlated insulating phases of twisted bilayer graphene at commensurate filling fractions: A Hartree-Fock study, Phys. Rev. B **102**, 035136 (2020).

[33] K. P. Nuckolls, M. Oh, D. Wong, B. Lian, K. Watanabe, T. Taniguchi, B. A. Bernevig, and A. Yazdani, Strongly correlated Chern insulators in magic-angle twisted bilayer graphene, Nature (London) **588**, 610 (2020).

[34] Y. Da Liao, J. Kang, C. N. Breiø, X. Y. Xu, H.-Q. Wu, B. M. Andersen, R. M. Fernandes, and Z. Y. Meng, Correlation-induced insulating topological phases at charge neutrality in twisted bilayer graphene, Phys. Rev. X **11**, 011014 (2021).

[35] X. Liu, Z. Wang, K. Watanabe, T. Taniguchi, O. Vafek, and J. Li, Tuning electron correlation in magic-angle twisted bilayer graphene using coulomb screening, Science **371**, 1261 (2021).

[36] A. T. Pierce, Y. Xie, J. M. Park, E. Khalaf, S. H. Lee, Y. Cao, D. E. Parker, P. R. Forrester, S. Chen, K. Watanabe *et al.*, Unconventional sequence of correlated Chern insulators in magic-angle twisted bilayer graphene, Nat. Phys. **17**, 1210 (2021).

[37] M. I. B. Utama, R. J. Koch, K. Lee, N. Leconte, H. Li, S. Zhao, L. Jiang, J. Zhu, K. Watanabe, T. Taniguchi *et al.*, Visualization of the flat electronic band in twisted bilayer graphene near the magic angle twist, Nat. Phys. **17**, 184 (2021).

[38] A. Ciarrocchi, F. Tagarelli, A. Avsar, and A. Kis, Excitonic devices with van der Waals heterostructures: Valleytronics meets twistronics, Nat. Rev. Mater. **7**, 449 (2022).

[39] J. An and J. Kang, Emergence and tuning of multiple flat bands in twisted bilayer γ-graphyne, J. Phys. Chem. Lett. **12**, 12283 (2021).

[40] X.-J. Zhao, Y. Yang, D.-B. Zhang, and S.-H. Wei, Formation of bloch flat bands in polar twisted bilayers without magic angles, Phys. Rev. Lett. **124**, 086401 (2020).

[41] M. H. Naik and M. Jain, Ultraflatbands and shear solitons in moiré patterns of twisted bilayer transition metal dichalcogenides, Phys. Rev. Lett. **121**, 266401 (2018).

[42] F. Wu, T. Lovorn, E. Tutuc, and A. H. MacDonald, Hubbard model physics in transition metal dichalcogenide moiré bands, Phys. Rev. Lett. **121**, 026402 (2018).

[43] F. Wu, T. Lovorn, E. Tutuc, I. Martin, and A. H. MacDonald, Topological insulators in twisted transition metal dichalcogenide homobilayers, Phys. Rev. Lett. **122**, 086402 (2019).

[44] D. A. Ruiz-Tijerina and V. I. Fal'ko, Interlayer hybridization and moiré superlattice minibands for electrons and excitons in heterobilayers of transition-metal dichalcogenides, Phys. Rev. B **99**, 125424 (2019).

[45] Z. Zhan, Y. Zhang, P. Lv, H. Zhong, G. Yu, F. Guinea, J. Á. Silva-Guillén, and S. Yuan, Tunability of multiple ultraflat bands and effect of spin-orbit coupling in twisted bilayer transition metal dichalcogenides, Phys. Rev. B **102**, 241106(R) (2020).

[46] L. Wang, E.-M. Shih, A. Ghiotto, L. Xian, D. A. Rhodes, C. Tan, M. Claassen, D. M. Kennes, Y. Bai, B. Kim *et al.*, Correlated electronic phases in twisted bilayer transition metal dichalcogenides, Nat. Mater. **19**, 861 (2020).

[47] H. Li, S. Li, M. H. Naik, J. Xie, X. Li, J. Wang, E. Regan, D. Wang, W. Zhao, S. Zhao *et al.*, Imaging moiré flat bands in three-dimensional reconstructed WSe_2/WS_2 superlattices, Nat. Mater. **20**, 945 (2021).

[48] X. Kuang, Z. Zhan, and S. Yuan, Flat-band plasmons in twisted bilayer transition metal dichalcogenides, Phys. Rev. B **105**, 245415 (2022).

[49] L. Rademaker, Spin-orbit coupling in transition metal dichalcogenide heterobilayer flat bands, Phys. Rev. B **105**, 195428 (2022).

[50] Z. Dai, L. Liu, and Z. Zhang, Strain engineering of 2D materials: Issues and opportunities at the interface, Adv. Mater. **31**, 1805417 (2019).

[51] Y. Qi, M. A. Sadi, D. Hu, M. Zheng, Z. Wu, Y. Jiang, and Y. P. Chen, Recent progress in strain engineering on van der Waals 2D materials: Tunable electrical, electrochemical, magnetic, and optical properties, Adv. Mater. **35**, 2205714 (2023).

[52] Y. Li, P. Chen, H. Liu, J. Peng, and N. Luo, The buckling behavior of single-layer MoS_2 sheets on silica substrates, J. Appl. Phys. **129**, 014302 (2021).

[53] Y. Han, P. Chen, C. Zhang, J. Dong, and H. Liu, The buckling behavior of single-layer MoS_2 sheets with Kirigami-inspired structures under compression, Comput. Mater. Sci. **188**, 110188 (2021).

[54] Y. Li, P. Chen, C. Zhang, J. Peng, F. Gao, and H. Liu, Molecular dynamics simulation on the buckling of single-layer MoS_2 sheet with defects under uniaxial compression, Comput. Mater. Sci. **162**, 116 (2019).

[55] W. Shi, Y. Guo, Z. Zhang, and W. Guo, Flexoelectricity in monolayer transition metal dichalcogenides, J. Phys. Chem. Lett. **9**, 6841 (2018).

[56] J. Qi, X. Li, X. Qian, and J. Feng, Bandgap engineering of rippled MoS_2 monolayer under external electric field, Appl. Phys. Lett. **102**, 173112 (2013).

[57] Q. Xu, Y. Guo, and L. Xian, Moiré flat bands in twisted 2D hexagonal vdW materials, 2D Mater. **9**, 014005 (2022).

[58] G. Pasquale, E. Lopriore, Z. Sun, K. Čerņevičs, F. Tagarelli, K. Watanabe, T. Taniguchi, O. V. Yazyev, and A. Kis, Electrical detection of the flat-band dispersion in van der Waals field-effect structures, Nat. Nanotechnol. **18**, 1416 (2023).

[59] S. Y. Lee, W. S. Yun, and J. D. Lee, Strain-induced dark exciton generation in rippled monolayer MoS_2, Phys. Chem. Chem. Phys. **25**, 9894 (2023).

[60] D. J. Trainer, Y. Zhang, F. Bobba, X. Xi, S.-W. Hla, and M. Iavarone, The effects of atomic-scale strain relaxation on the electronic properties of monolayer MoS_2, ACS Nano **13**, 8284 (2019).

[61] A. P. Thompson, H. M. Aktulga, R. Berger, D. S. Bolintineanu, W. M. Brown, P. S. Crozier, P. J. in't Veld, A. Kohlmeyer, S. G. Moore, T. D. Nguyen *et al.*, LAMMPS-a flexible simulation tool for particle-based materials modeling at the atomic, meso, and continuum scales, Comput. Phys. Commun. **271**, 108171 (2022).

[62] D. W. Brenner, Empirical potential for hydrocarbons for use in simulating the chemical vapor deposition of diamond films, Phys. Rev. B **42**, 9458 (1990).

[63] D. W. Brenner, O. A. Shenderova, J. A. Harrison, S. J. Stuart, B. Ni, and S. B. Sinnott, A second-generation reactive empirical bond order (REBO) potential energy expression for hydrocarbons, J. Phys.: Condens. Matter **14**, 783 (2002).

[64] J. M. Soler, E. Artacho, J. D. Gale, A. García, J. Junquera, P. Ordejón, and D. Sánchez-Portal, The SIESTA method for *ab initio* order-n materials simulation, J. Phys.: Condens. Matter **14**, 2745 (2002).

[65] J. P. Perdew, K. Burke, and M. Ernzerhof, Generalized gradient approximation made simple, Phys. Rev. Lett. **77**, 3865 (1996).

[66] See Supplemental Material at http://link.aps.org/supplemental/10.1103/PhysRevMaterials.9.L021002 for additional band structures and electronic structure calculations of WS_2, $MoSe_2$, and WSe_2, including detailed effective mass calculations, probability density distributions for states at the valence band maximum and conduction band minimum, and comparative

band structure evolution under compression for all studied TMDs. The Supplemental Material also contains Refs. [68,69].

[67] L. Wang, Z. Fu, J. Sun, M. Liu, W. Yi, C. Yi, Y. Luo, Y. Dai, G. Liu, Y. Matsushita, K. Yamaura, L. Lu, J.-G. Cheng, Y.-F. Yang, Y. Shi, and J. Luo, Heavy fermion behavior in the quasi-one-dimensional Kondo lattice $CeCo_2Ga_8$, npj Quantum Mater. **2**, 36 (2017).

[68] T. Liang, S. R. Phillpot, and S. B. Sinnott, Parametrization of a reactive many-body potential for Mo–S systems, Phys. Rev. B **79**, 245110 (2009).

[69] J. A. Stewart and D. E. Spearot, Atomistic simulations of nanoindentation on the basal plane of crystalline molybdenum disulfide (MoS_2), Modell. Simul. Mater. Sci. Eng. **21**, 045003 (2013).